

Mining for Dark Matter Substructure: Inferring subhalo population properties from strong lenses with machine learning


JOHANN BREHMER,^{1,2} SIDDHARTH MISHRA-SHARMA,¹ JOERI HERMANS,³ GILLES LOUPPE,³ AND KYLE CRANMER^{1,2}

¹*Center for Cosmology and Particle Physics, Department of Physics, New York University, 726 Broadway, New York, NY 10003, USA*

²*Center for Data Science, New York University, 60 Fifth Ave, New York, NY 10011, USA*

³*Montefiore Institute, University of Liège, Belgium*

ABSTRACT

The subtle and unique imprint of dark matter substructure on extended arcs in strong lensing systems contains a wealth of information about the properties and distribution of dark matter on small scales and, consequently, about the underlying particle physics. However, teasing out this effect poses a significant challenge due to the high dimensionality of the underlying latent space associated with a large number of dark matter subhalos. We apply recently-developed simulation-based techniques to the problem of substructure inference in galaxy-galaxy strong lenses. By leveraging additional information extracted from the simulator, these methods can be used to train neural networks to estimate likelihood ratios associated with population-level parameters characterizing substructure. We show through proof-of-principle application to simulated data that these methods can provide an efficient and principled way to concurrently analyze an ensemble of strong lenses, and can be used to mine the large sample of lensing images deliverable by future surveys for signatures of dark matter substructure. 

Keywords: strong gravitational lensing (1643) — gravitational lensing (670) — nonparametric inference (1903) — astrostatistics techniques (1886) — cosmology (343) — dark matter (353)

Contents		3.4. Inference	10
1. Introduction	1	4. Results	10
2. Strong lensing formalism and simulation setup	3	5. Extensions	12
2.1. Strong lensing formalism	3	6. Conclusions	14
2.2. Lensing host galaxy	4	A. Minimum of the loss functional	15
2.3. Background source	4	B. Simplified scenarios	16
2.4. Lensing substructure	5		
2.5. Observational considerations	6		
2.6. Population statistics of the lens and source samples	6		
3. Statistical formalism and simulation-based inference	6		
3.1. Extracting additional information from the simulator	8		
3.2. Machine learning	9		
3.3. Calibration	10		

1. INTRODUCTION

Dark matter (DM) accounts for nearly a quarter of the energy budget of the Universe, and pinning down its fundamental nature and interactions is one of the most pressing problems in cosmology and particle physics today. Despite an organized effort to do so through terrestrial (Aprile et al. 2018; Cui et al. 2017; Akerib et al. 2017), astrophysical (Albert et al. 2017; Chang et al. 2018; Lisanti et al. 2018), and collider searches (Aaboud et al. 2019; Sirunyan et al. 2017), no conclusive evidence of interactions between the Standard Model (SM) and dark matter exists to-date.

An alternative and complementary approach involves studying dark matter directly through its irreducible gravitational interactions. The concordance Cold Dark Matter (CDM) framework of non-relativistic, collisionless dark matter particles provides an excellent description of the observed distribution of matter on large scales. However, many well-motivated models predict deviations from CDM on smaller scales. Fundamental dark matter microphysical properties, such as its particle mass and self-interaction cross-section, can imprint themselves onto its macroscopic distribution in ways that can be probed by current and future experiments (Drlica-Wagner et al. 2019; Buckley & Peter 2018). As motivating examples, theories where dark matter has a significant free-streaming length would lead to a dearth of subhalos at lower masses ($\lesssim 10^9 M_\odot$) (Bond & Szalay 1983; Bode et al. 2001; Dalcanton & Hogan 2001; Boyanovsky et al. 2008; Boyanovsky & Wu 2011), and self-interactions (Kaplinghat et al. 2016, 2014; Zavala et al. 2013; Peter et al. 2013; Vogelsberger et al. 2012, 2019; Kahlhoefer et al. 2019) or dissipative dynamics (Agrawal & Randall 2017; Agrawal et al. 2017; Buckley & DiFranzo 2018; Fan et al. 2013; Vogelsberger et al. 2016) in the dark sector would modify the structure of the inner core of subhalos as compared to CDM predictions.

There exist several avenues for probing the distribution of dark matter on small scales. While the detection of ultrafaint dwarf galaxies through the study of stellar overdensities and kinematics (Bechtol et al. 2015; Koposov et al. 2008, 2015) can be used to make statements about the underlying dark matter properties, theoretical uncertainties in the connection between stellar and halo masses (Nadler et al. 2019; Wechsler & Tinker 2018) and the effect of baryons on the satellite galaxy population (Brooks 2018; Fitts et al. 2018; Garrison-Kimmel et al. 2017; Errani et al. 2017) pose a challenge. Furthermore, suppressed star-formation in smaller halos means that there exists a threshold ($\lesssim 10^8 M_\odot$) below which subhalos are expected to be mostly dark and devoid of baryonic activity (Efstathiou 1992; Fitts et al. 2017; Read et al. 2017). This makes studying the imprints of gravitational interaction the *only* viable avenue for probing substructure at smaller scales. In this spirit, the study of subhalo-induced perturbations to the kinematic phase-space distribution in cold stellar streams (Bonaca & Hogg 2018; Johnston et al. 1999; Carlberg 2012; Carlberg & Grillmair 2013; Bonaca et al. 2019), and in Galactic stellar fields (Buschmann et al. 2018) have been proposed as methods to look for low-mass subhalos through their gravitational interactions in the Milky Way.

Complementary to the study of locally-induced gravitational effects, gravitational lensing has emerged as an important tool for studying the distribution of matter over a large range of scales. Locally, the use of time-domain astrometry has been proposed as a promising method to measure the distribution of local substructure through correlated, lens-induced motions of background celestial objects due to foreground subhalos (Van Tilburg et al. 2018). In the extragalactic regime, galaxy-scale strong lensing systems are a laboratory for studying substructure. The presence of flux-ratio anomalies in multiply-imaged quasar lenses has been used to infer the typical abundance of substructure within galaxy-scale lenses (Dalal & Kochanek 2002; Hsueh et al. 2019; Dalal & Kochanek 2002) and lensed images of extended sources have been used to find evidence for a handful of subhalos with masses $\gtrsim 10^8 M_\odot$ (Hezaveh et al. 2016b; Vegetti et al. 2010, 2012).

Another approach relies on probing the collective effect of sub-threshold (i.e., not individually resolvable) subhalos on extended arcs in strongly lensed systems. A particular challenge here is the high dimensionality of the latent parameter space associated with the large number of subhalos and their individual as well as population properties. An immediate consequence of this fact is the intractability of calculating the likelihood of high-level substructure parameters conditional on data. Methods based on summary statistics (Birrer et al. 2017a) and studying the amplitude of spatial fluctuations on different scales through power spectra (Hezaveh et al. 2016a; Díaz Rivero et al. 2018; Díaz Rivero et al. 2018; Cyr-Racine et al. 2019; Brennan et al. 2019; Chatterjee & Koopmans 2018; Cyr-Racine et al. 2016) have been proposed as ways to reduce the dimensionality of the problem and enable substructure inference in a tractable way. Trans-dimensional techniques may also be able to efficiently map out the parameter space associated with multiple sub-threshold subhalos in these systems (Brewer et al. 2016; Daylan et al. 2018). This class of methods is well-suited to studying dark matter substructure since they can be sensitive to the *population* properties of low-mass subhalos in strongly lensed galaxies which are directly correlated with the underlying dark matter particle physics. Furthermore, near-future observatories like DES (Dark Energy Survey Collaboration et al. 2016), LSST (LSST Science Collaboration et al. 2009; Drlica-Wagner et al. 2019; Verma et al. 2019), and *Euclid* (Refregier et al. 2010) are expected to find hundreds to thousands of galaxy-galaxy strong lenses (Collett 2015; Oguri & Marshall 2010; Treu 2010), making substructure inference in these systems (and high-resolution followups on a subset) one of the

key avenues for investigating dark matter substructure and stress-testing the Cold Dark Matter paradigm in the near future. This calls for methods that can efficiently analyze large samples of lensed images to infer the underlying substructure properties with minimal loss of information stemming from dimensional reduction.

In recent years, a large number of methods have been developed that train neural networks to estimate the likelihood function, likelihood ratio function, or posterior (Fan et al. 2012; Dinh et al. 2014; Germain et al. 2015; Jimenez Rezende & Mohamed 2015; Cranmer et al. 2015; Paige & Wood 2016; Uria et al. 2016; Dinh et al. 2016; van den Oord et al. 2016b,c,a; Thomas et al. 2016; Papamakarios & Murray 2016; Tran et al. 2017; Papamakarios et al. 2017; Louppe & Cranmer 2017; Lueckmann et al. 2017; Gutmann et al. 2017; Huang et al. 2018; Papamakarios et al. 2018; Lueckmann et al. 2018; Chen et al. 2018; Kingma & Dhariwal 2018; Grathwohl et al. 2018; Dinev & Gutmann 2018; Hermans et al. 2019; Alsing et al. 2019). In contrast to traditional simulation-based (or “likelihood-free”) approaches, these methods do not rely on summary statistics and instead learn to extract information directly from the full input data, which in our case corresponds to the observed lensed images. These approaches let us to amortize the computational cost of the inference: after an upfront simulation and training phase, inference for any observed lens image is efficient, enabling a stacked analysis of a large number of observations.

We follow this approach and apply a particularly efficient technique for simulation-based inference (Brehmer et al. 2018a,b,c; Stoye et al. 2018) to the problem of extracting high-level substructure properties from an ensemble of galaxy-galaxy strong lensing images. This method extracts additional information from the simulator, which is then used to train a neural network as a surrogate for the likelihood ratio function. Compared to other neural-network-based methods, the additional information increases the sample efficiency and thus reduces the computational cost. A calibration procedure ensures correct inference results even in the case of imperfectly trained networks.

We demonstrate the feasibility of this method on a catalog of simulated lenses. After discussing the information in individual lens images, we switch to a stacked analysis of multiple observed images and calculate the expected limits on population-level substructure parameters in both a frequentist and a Bayesian setup.

This paper is organized as follows. In Sec. 2 we briefly review the formalism of gravitational strong lensing and describe our simulation setup, including the assumptions we make about the population of lensed sources and host

galaxies, the substructure population and observational parameters. In Sec. 3 we describe the simulation-based analysis technique used and its particular application to the problem of mining dark matter substructure properties from an ensemble of extended lensed arcs. We show a proof-of-principle application of this method to simulated data in Sec. 4 and comment on how these methods can be extended to more realistic scenarios in Sec. 5. We conclude in Sec. 6.

2. STRONG LENSING FORMALISM AND SIMULATION SETUP

In strong lensing systems, the background light emission source can in general be a point-like quasar or supernova, or a faint, extended “blue” galaxy. The former results in multiple localized images on the lens plane rather than extended arc-like images, providing the ability to probe substructure over a limited region on the lens plane. For this reason, we focus our method towards galaxy-galaxy lenses—systems producing images with extended arcs—since we aim to disentangle the collective effect of a population of subhalo perturbers over multiple images. Young, blue galaxies are ubiquitous in the redshift regime $z \gtrsim 1$ and dominate the faint end of the galaxy luminosity function, resulting in a much larger deliverable sample of galaxy-galaxy strong lenses compared to multiply-imaged quasars or supernovae.

We now briefly review the basic mathematical formalism behind strong lensing before describing in turn the models for the background source, lensing galaxy and population parameters of the lens systems used in this study. For more details on the formalism see, e.g., Keeton (2001); Schneider et al. (1992); Treu (2010).

2.1. Strong lensing formalism

For a mass distribution with dimensionless projected surface mass density $\kappa(\mathbf{r}) \equiv \Sigma(\mathbf{r})/\Sigma_{\text{cr}}$, where $\Sigma_{\text{cr}} \equiv \frac{1}{4\pi G_N} \frac{D_s}{D_l D_s}$ is the critical lensing surface density and D_l , D_s , and D_{ls} are the observer-lens, observer-source and lens-source angular diameter distances, respectively, the two-dimensional projected lensing potential is given by

$$\psi(\mathbf{r}) = \frac{1}{\pi} \int d\mathbf{r}' \ln |\mathbf{r} - \mathbf{r}'| \kappa(\mathbf{y}). \quad (1)$$

The lensed position of the source \mathbf{r} can be determined through the lens equation,

$$\mathbf{u} = \mathbf{r} - \nabla\psi(\mathbf{r}) \quad (2)$$

where \mathbf{u} is the position of the source and $\nabla\psi$ is typically referred to as the deflection, which we will denote as ϕ for brevity. For an extended source brightness profile

f_{src} , the final lensed image can be obtained as the source profile evaluated on the image plane,

$$f'_{\text{src}}(\mathbf{r}) = f_{\text{src}}(\mathbf{r} - \nabla\psi(\mathbf{r})). \quad (3)$$

For a spherically symmetric halo, the radial deflection field is given by

$$\phi_r(r) = \frac{2}{r} \int_0^r dr' r' \kappa(r') = \frac{1}{\pi \Sigma_{\text{cr}}} \frac{M_{\text{cyl}}(r)}{r}, \quad (4)$$

where $M_{\text{cyl}}(r)$ is the mass enclosed within a cylinder of radius r . Extension to the slightly more general case of elliptical symmetry is straightforward (see, e.g., [Keeton \(2001\)](#)).

2.2. Lensing host galaxy

Cosmological N -body simulations suggest that the dark matter distribution in structures at galactic scales can be well-described by a universal, spherically symmetric Navarro-Frenk-White (NFW) profile. However, strong lensing probes a region of the host galaxy much smaller than the typical virial radii of galaxy-scale dark matter halo, and the mass budget here is dominated by the baryonic bulge component of the galaxy. Taking this into account, the total mass budget of the lensing host galaxy, being early-type, can be well-described by a singular isothermal ellipsoid (SIE) profile. Since neither the dark matter nor the baryonic components are individually isothermal, this is known as the bulge-halo conspiracy ([Treu 2010](#)). The profile of an SIE halo is given by

$$\rho_{\text{SIE}}(\theta_x, \theta_y) = \frac{\sigma_v^2}{2\pi G_N (\theta_x^2/q + q\theta_y^2)} \quad (5)$$

where σ_v is the central 1-D velocity dispersion of the lens galaxy and q is the ellipsoid axis ratio, with $q = 1$ corresponding to a spherical profile. We explicitly denote our angular coordinates as $\{\theta_x, \theta_y\}$. The Einstein radius for this profile, defining the characteristic lensing scale, is given by

$$\theta_E = 4\pi \left(\frac{\sigma_v}{c}\right)^2 \frac{D_{ls}(z_l, z_s)}{D_s(z_s)}, \quad (6)$$

where z_l and z_s are respectively the lens and source redshifts. We use the cosmology from [Planck Collaboration et al. \(2016\)](#) to compute cosmological distances throughout this paper.

The deflection field for the SIE profile is given by ([Keeton 2001](#))

$$\phi_x = \frac{\theta_E q}{\sqrt{1-q^2}} \tan^{-1} \left[\frac{\sqrt{1-q^2}\theta_x}{\chi} \right] \quad (7)$$

$$\phi_y = \frac{\theta_E q}{\sqrt{1-q^2}} \tanh^{-1} \left[\frac{\sqrt{1-q^2}\theta_y}{\chi + q^2} \right] \quad (8)$$

with $\chi \equiv \sqrt{\theta_x^2 q^2 + \theta_y^2}$.

Although the total galaxy mass (baryons + dark matter) describe the macro lensing field, for the purposes of describing substructure we require being able to map the measure properties of an SIE lens onto the properties of the host dark matter halo. To do this, we relate the central stellar velocity dispersion σ_v to the mass M_{200} of the host dark matter halo. [Zahid et al. \(2018\)](#) derived a tight correlation between σ_v and M_{200} , modeled as

$$\log \left(\frac{M_{200}}{10^{12} \text{M}_\odot} \right) = \alpha + \beta \left(\frac{\sigma_v}{100 \text{km s}^{-1}} \right) \quad (9)$$

with $\alpha = 0.09$ and $\beta = 3.48$. We model the host dark matter halo with an NFW profile ([Navarro et al. 1996, 1997](#))

$$\rho_{\text{NFW}}(r) = \frac{\rho_s}{(r/r_s)(1+r/r_s)^2} \quad (10)$$

where ρ_s and r_s are the scale density and scale radius, respectively. The halo virial mass M_{200} describes the total mass contained within the virial radius r_{200} , defined as the radius within which the mean density is 200 times the critical density of the universe and related to the scale radius through the concentration parameter $c_{200} \equiv r_{200}/r_s$. Thus, an NFW halo is completely described by the parameters $\{M_{200}, c_{200}\}$. We use the concentration model from [Sánchez-Conde & Prada \(2014\)](#) to derive the halo concentration for a given NFW virial mass.

The spherically-symmetric deflection for an NFW perturber is given by ([Keeton 2001](#))

$$\phi_r = 4\kappa_s r_s \frac{\ln(x/2) + \mathcal{F}(x)}{x}, \quad (11)$$

where $x \equiv r/r_s$, $\kappa_s \equiv \rho_s r_s / \Sigma_{\text{cr}}$ with the critical surface density Σ_{cr} , and

$$\mathcal{F}(x) = \begin{cases} \frac{1}{\sqrt{x^2-1}} \tan^{-1} \sqrt{x^2-1} & (x > 1) \\ \frac{1}{\sqrt{1-x^2}} \tanh^{-1} \sqrt{1-x^2} & (x < 1) \\ 1 & (x = 1). \end{cases} \quad (12)$$

We described the population parameters used to model the host velocity dispersion (and thus its Einstein radius and dark matter halo mass) in Secs. 2.5 and 2.6 below.

2.3. Background source

We model the emission from background source galaxies using a Sérsic profile, with the surface brightness given by ([Sérsic 1963](#))

$$f_{\text{src}}(\theta_r) = f_e \exp \left\{ -b_n \left[\left(\frac{\theta_r}{\theta_{r,e}} \right)^{1/n} - 1 \right] \right\}, \quad (13)$$

where $\theta_{r,e}$ is the effective circular half-light radius, n is the Sérsic index, and b_n is a factor depending on n that ensures that $\theta_{r,e}$ contains half the total intensity from the source galaxy, given by (Ciotti & Bertin 1999)

$$b_n \approx 2n - \frac{1}{3} + \frac{4}{405n} + \frac{46}{25515n^2} + \frac{131}{1148175n^3} - \frac{2194697}{30690717750n^4}.$$

We assume $n = 1$ for the source galaxies, corresponding to a flattened exponential profile and consistent with expectation for blue-type galaxies at the relevant redshifts. f_e encodes the flux at half-light radius, which can be inferred from the total flux (or magnitude) associated with a given galaxy as follows. For a detector with zero-point magnitude M_0 , which specifies the magnitude of a source giving 1 counts s^{-1} in expectation, by definition the total counts are given by $S_{\text{tot}} = 10^{0.4(M-M_0)}$. Requiring the half-light radius to contain half the expected counts, for $n = 1$ we have the relation $f_e \approx 0.526 t_{\text{exp}} S_{\text{tot}} / (2\pi\theta_{r,e}^2)$ in counts arcsec^{-2} , where t_{exp} is the exposure length.

The treatment of the other Sérsic parameters, in particular the total emission and half-light radius, in the context of population studies is described in Sec. 2.6 below.

2.4. Lensing substructure

The ultimate goal of our method is to characterize the substructure population in strong lenses. Here we describe our procedure to model the substructure contribution to the lensing signal. Understanding the expected abundance of substructure in galaxies over a large range of epochs is a complex problem and an active ongoing area of research. Properties of individual subhalos (such as their density profiles) as well as those that describe their population (such as the mass and spatial distribution) are strongly affected by their host environment, and accurately modeling all aspects of subhalo evolution and environment is beyond the scope of this paper. Instead, we use a simplified description to model the substructure contribution in order to highlight the broad methodological points associated with the application of our method.

A Cold Dark Matter (ACDM), often called the standard model of cosmology, predicts a scale-invariant power spectrum of primordial fluctuations and the existence of substructure over a broad range of masses with approximately equal contribution per logarithmic mass interval. We parameterize the distribution of subhalo masses m_{200} in a given host halo of mass M_{200} —the subhalo mass function—as a power law distribution with a

linear dependence on the host halo mass,

$$\frac{dn}{d \log \frac{m_{200}}{m_{200,0}}} = \begin{cases} \alpha \frac{M_{200}}{M_{200,0}} \left(\frac{m_{200}}{m_{200,0}} \right)^\beta & (m_{200}^{\min} \leq m_{200} \leq m_{200}^{\max}) \\ 0 & (\text{else}), \end{cases} \quad (14)$$

where α encodes the overall substructure abundance, with larger α corresponding to more substructure, and the slope $\beta < 0$ encodes the relative contribution of subhalos at different masses, with more negative β corresponding to a steeper slope with more low-mass subhalos. $m_{200,0}$ and $M_{200,0}$ are arbitrary normalization factors.

Theory and simulations within the framework of Λ CDM predict a slope $\beta \approx -0.9$ (Springel et al. 2008; Madau et al. 2008), resulting in nearly scale-invariant spectrum of subhalos, which we assume in our fiducial setup. We parameterize the overall subhalo abundance α through the mass fraction within the lensing galaxies contained in subhalos, f_{sub} , defined as the fraction of the total dark matter halo mass contained in bound substructure in a given mass range:

$$f_{\text{sub}} = \frac{\int_{m_{200,\min}}^{m_{200,\max}} dm_{200} m_{200} \frac{dn}{dm_{200}}}{M_{200}}. \quad (15)$$

For a given $\{f_{\text{sub}}, \beta\}$ and host halo mass M_{200} , this can be used to determine α in Eq. (14). The linear scaling of the subhalo mass function with the host halo mass M_{200} in Eq. (14) is additionally described in Han et al. (2016); Despali & Vegetti (2017). In our fiducial setups, we take the minimum mass $m_{200,\min} = 10^7 M_\odot$ and $m_{200,\max} = 0.01 M_{200}$ (Despali & Vegetti 2017; Hiroshima et al. 2018), and corresponding fiducial substructure mass fraction in this range of 5%, roughly consistent with Hiroshima et al. (2018); Hsueh et al. (2019); Dalal & Kochanek (2002).

With all parameters of the subhalo mass function specified, the total number of subhalos \bar{n}_{tot} expected within the virial radius R_{200} of the host halo can be inferred as $\int_{m_{200,\min}}^{m_{200,\max}} dm_{200} \frac{dn}{dm_{200}}$. Strong lensing probes a region much smaller than this scale—the typical Einstein radii for the host deflector are much smaller than the virial radius of the host dark matter halos. In order to obtain the expected number of subhalos within the lensing observations region of interest (ROI), we scale the total number of subhalos obtained from the above procedure by the ratio of projected mass within our region of interest θ_{ROI} and the host halo mass M_{200} as follows. We assume the subhalos to be distributed in number density following the host NFW dark matter profile. In this case, the enclosed mass function is $M_{\text{enc}}(x) = M_{200} [\ln(x/2) + \mathcal{F}(x)]$ (Keeton 2001), where

x is the angular radius in units of the scale radius, $x \equiv \theta/\theta_s$ and $\mathcal{F}(x)$ is given by Eq. (12) above. The expected number of subhalos within our ROI is thus obtained as $\bar{n}_{\text{ROI}} = \bar{n}_{\text{tot}} [\ln(x_{\text{ROI}}/2) + \mathcal{F}(x_{\text{ROI}})]$. We conservatively take the lensing ROI to enclose a region of angular size twice the Einstein radius of the host halo, $\theta_{\text{ROI}} = 2 \cdot \theta_E$.

Since strong lensing probes the line-of-sight distribution of subhalos within the host, their projected spatial distribution is approximately uniform within the lensing ROI (Despali & Vegetti 2017). We thus distribute subhalos uniformly within our ROI. The density profile of subhalos is assumed to be NFW and given by Eq. (10), with associated lensing properties as described and the concentration inferred using the model in Sánchez-Conde & Prada (2014).

We finally emphasize that we do not intent to capture all of the intricacies of the subhalo distribution, such as the effects of baryonic physics, tidal disruption of subhalos in proximity to the center of the host and redshift evolution of host as well as substructure properties. Although our description can be extended to take these into account (see Sec. 5), their precise characterization and effect is still subject to large uncertainties, and our simple model above captures the essential physics for demonstration purposes.

2.5. Observational considerations

As noted above, our method is best-suited to analyzing a statistical sample of strong lenses, such as those that are expected to be obtained in the near future with optical telescopes like *Euclid* and LSST, to quantify the effect of substructure. Given the challenges associated with the precise characterization of such a sample at the present time, we describe here the observational characteristics we assume in order to build up training and testing samples to validate our inference techniques.

We largely follow the description of Collett (2015), and use the associated *LensPop* package, to characterize our mock observations. In particular, we use the nominal detector configuration for *Euclid*, assuming a zero-point magnitude $m_{\text{AB}} = 25.5$ in the single optical VIS passband, pixel size 0.1 arcsec, a Gaussian point spread function (PSF) with FWHM 0.18 arcsec, individual exposures with exposure time 1610 s, and an isotropic sky background with magnitude 22.8 arcsec^{-2} in the detector passband.

These properties, in particular the exposure, sky background, and PSF shape, are expected to vary somewhat across the lens sample. Additionally, a given region may be imaged by multiple exposures over a range of color bands. Although such variations can easily be incorpo-

rated into our analysis (see Sec. 5), modeling these is beyond the scope of this study. We comment on how this information can be taken into account in Sec. 5.

2.6. Population statistics of the lens and source samples

The fact that the strong lens population is expected to be dominated by higher-redshift ($z_s \gtrsim 1$) blue source galaxies lensed by intermediate-redshift ($z_l \sim 0.5\text{--}1$) elliptical galaxies presents significant challenges for quantifying the lens population obtainable with future observations. Specifically, planned ground-based surveys like LSST and space telescopes like *Euclid* present complementary challenges for delivering images of strong lensing systems suitable for substructure studies. LSST is expected to image in six bands, allowing efficient source selection and distinguishing source and lens emission, but at the cost of lower resolution by virtue of being a ground-based instrument. *Euclid* imaging is expected to be much higher in resolution but with a single optical passband (VIS). Near-IR imaging from WFIRST may deliver a high-resolution, multi-wavelength dataset that is more suitable for substructure studies, although the lens and source populations may differ from those probed by optical telescopes.

In light of these uncertainties, we confine ourselves to a setting where the main methodological points can be made without detailed modeling of the detector capabilities and the deliverable lensing dataset, which is outside of the scope of the current paper. For concreteness, we simulate a sample of lenses with a simplified subset of host galaxy properties consistent with those deliverable by *Euclid* as modeled by Collett (2015). In particular, we assume spherical lenses, with ellipticity parameter $q = 1$ in Eq. (5). We draw the central 1-D velocity dispersions σ_v of host galaxies from a normal distribution with mean 225 km s^{-1} and standard deviation 50 km s^{-1} . Following Zahid et al. (2018), Eq. (9) is used to map the drawn σ_v to a dark matter halo mass M_{200} , and the host Einstein radius is analytically inferred with Eq. (6).

We draw the lens redshifts z_l from a log-normal distribution with mean 0.56 and scatter 0.25 dex, discarding lenses with $z_l > 1$ as these tend to have a small angular size over which substructure perturbations are relevant. The source redshift is fixed at $z_s = 1.5$, its offsets θ_x and θ_y are drawn from a normal distribution with zero mean and standard deviation 0.2. These choices are consistent with the lens sample generated from the *LensPop* code packaged with Collett (2015).

3. STATISTICAL FORMALISM AND SIMULATION-BASED INFERENCE

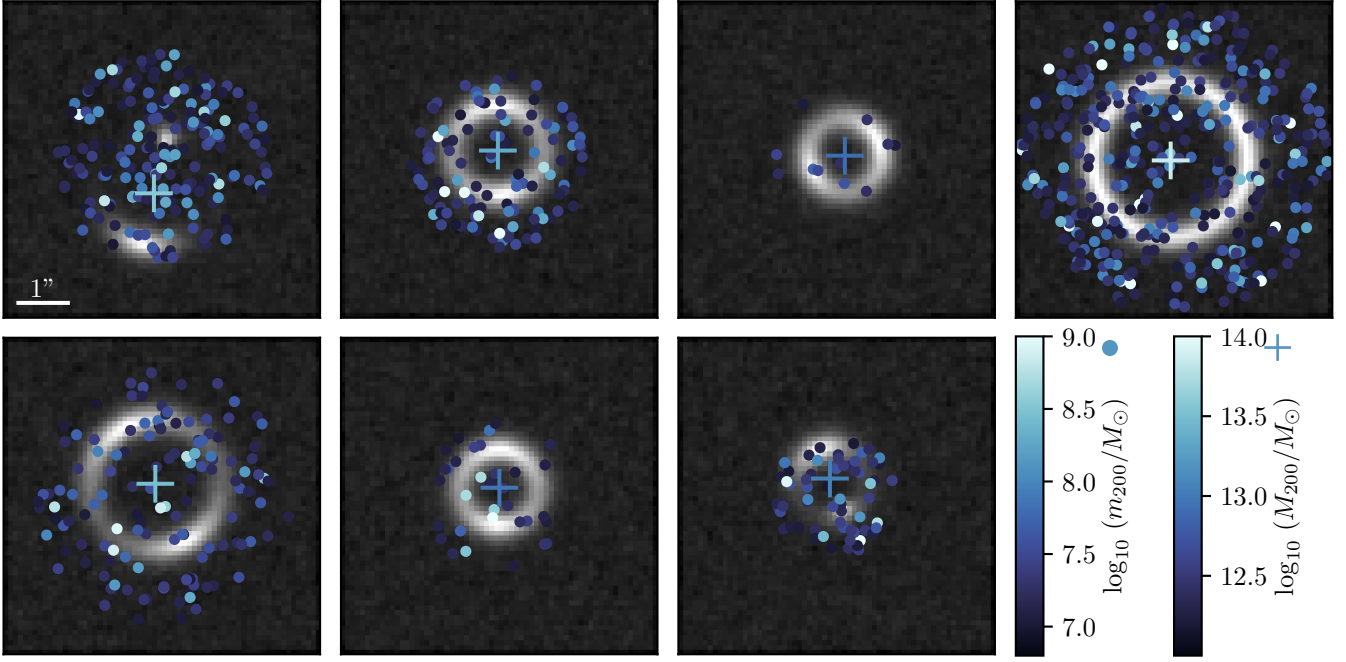


Figure 1. A sample of simulated lenses. The cross markers show the offset between the host and source centers, the color corresponding to the virial mass of the host dark matter halo. The simulated subhalos are shown as dots, the color again indicates their masses. The greyscale images show the corresponding observed images. We show seven images randomly generated for $f_{\text{sub}} = 0.05$ and $\beta = -0.9$.

Our goal is to infer the subhalo mass function parameters from a catalog of images of observed lenses. In this section we will describe the challenges of this inference problem and our approach of simulation-based inference. For simplicity, we will use a more abstract notation, distinguishing between three sets of quantities in the lensing system:

Parameters of interest ϑ : The vector $\vartheta = (f_{\text{sub}}, \beta)^T$ parameterizes the subhalo mass function given, and our goal is to infer their values.

Latent variables z : A vector of all other unobservable random variables in the simulator. These include the mass M_{200} , offset (θ_x, θ_y) , and redshift z_l of the lens, the number of subhalos in the region of interest n_{ROI} , the position \mathbf{r} and mass m_{200} of each subhalo, and the random variables related to the point spread function and Poisson fluctuations.

Observables x : The observed lens images.

Unfortunately, the same symbols are used with different meanings in astrophysics and statistics: note the difference between the parameters ϑ and the angular positions θ_x, θ_y and the Einstein radius θ_E ; between the latent variables z and the redshifts z_s, z_l ; and between the observed image x and the argument of the NFW profile $M_{\text{enc}}(x)$ and $\mathcal{F}(x)$ used in the last section.

As described above, we have implemented a simulator for the lensing process in the “forward” direction: for given parameters ϑ , the simulator samples latent variables z and finally observed images $x \sim p(x|\vartheta)$. Here $p(x|\vartheta)$ is the probability density or likelihood function of observing a lens image x given parameters ϑ . It can be schematically written as

$$p(x|\vartheta) = \int dz p(x, z|\vartheta), \quad (16)$$

where we integrate over the latent variables z and $p(x, z|\vartheta)$ is the joint likelihood of observables and latent variables:

$$\begin{aligned} p(x, z|\vartheta) &= p_{\text{host}}(M_{200}, \theta_x, \theta_y, z_l) \\ &\times \text{Pois}(n_{\text{ROI}}|\bar{n}_{\text{ROI}}(\vartheta)) \prod_i^{n_{\text{ROI}}} \left[p_m(m_{200,i}|\vartheta) \text{Uniform}(\mathbf{r}_i) \right] \\ &\times p_{\text{obs}}(x|f(M_{200}, \theta_x, \theta_y, z_l; \{(m_{200,i}, \mathbf{r}_i)\})). \end{aligned} \quad (17)$$

Here $p_{\text{host}}(M_{200}, \theta_x, \theta_y, z_l)$ is the distribution of the host halo parameters; $\bar{n}_{\text{ROI}}(\vartheta)$ is the mean number of subhalos in the region of interest as a function of the parameters $\vartheta = (f_{\text{sub}}, \beta)^T$, while n_{ROI} is the actually realized number in the simulation; $m_{200,i}$ and \mathbf{r}_i are the subhalo masses and positions; $p_m(m|\vartheta) = 1/n \, dn/dm_{200}$ is the normalized subhalo mass function given in Eq. (14); and

in the last line p_{obs} is the probability of observing an image x based on the true lensed image $f(z_l, \{(m_{200,i}, r_i)\})$ taking into account Poisson fluctuations and detector response through the point spread function.

Standard frequentist and Bayesian inference methods rely on evaluating the likelihood function $p(x|\vartheta)$. Unfortunately, even in our somewhat simplified simulator each run of the simulation easily involves hundreds to thousands of latent variables, the integral over this enormous space clearly cannot be computed explicitly. The likelihood function $p(x|\vartheta)$ is thus intractable, providing a major challenge for both frequentist and Bayesian inference. Similarly, inference with Markov Chain Monte Carlo (MCMC) methods based directly on the joint likelihood function $p(x, z|\vartheta)$ requires unfeasibly many samples before converging because the latent space is so large. Systems defined through a forward simulator that does not admit a tractable likelihood are known as “implicit models”, inference techniques for this case as “simulation-based inference” or “likelihood-free inference”.

One way to tackle this issue is to reduce the high-dimensional data x to lower-dimensional summary statistics $v(x)$, for instance based on power spectra (Hezaveh et al. 2016a; Díaz Rivero et al. 2018; Díaz Rivero et al. 2018; Cyr-Racine et al. 2019; Brennan et al. 2019; Chatterjee & Koopmans 2018; Cyr-Racine et al. 2016). The likelihood $p(v|\vartheta)$ in the space of summary statistics can either be explicitly estimated through density estimation techniques such as histograms, kernel density estimation, or Gaussian processes, or replaced by a rejection probability in an Approximate Bayesian Computation (ABC) technique (Rubin 1984). Substructure inference in quasar and extended-arc lenses using ABC techniques was explored in Gilman et al. (2018) and Birrer et al. (2017a), respectively. While the compression to summary statistics makes the analysis tractable, it typically loses information and hence reduces the statistical power of the analysis.

Instead, we follow an approach in which we approximate the likelihood function with a neural network, which has to be trained only once and can be evaluated efficiently for any parameter point and observed image (Fan et al. 2012; Dinh et al. 2014; Germain et al. 2015; Jimenez Rezende & Mohamed 2015; Cranmer et al. 2015; Paige & Wood 2016; Uria et al. 2016; Dinh et al. 2016; van den Oord et al. 2016b,c,a; Thomas et al. 2016; Papamakarios & Murray 2016; Tran et al. 2017; Papamakarios et al. 2017; Louppe & Cranmer 2017; Lueckmann et al. 2017; Gutmann et al. 2017; Huang et al. 2018; Papamakarios et al. 2018; Lueckmann et al. 2018; Chen et al. 2018; Kingma & Dhariwal 2018; Grath-

wohl et al. 2018; Dinev & Gutmann 2018; Hermans et al. 2019; Alsing et al. 2019). We will show how this turns the intractable integral in Eq. (16) into a tractable minimization problem and amortizes this marginalization. This approach scales well to the expected large number of lenses expected in upcoming surveys (Collett 2015; Oguri & Marshall 2010; Treu 2010). Since the full image is used as input, no information is lost due to dimensionality reduction.

We use a simulation-based inference technique introduced in Brehmer et al. (2018a,b,c) that extracts additional information from the simulation and uses it to improve the sample efficiency of the training of the neural network. Our inference strategy consists of four steps:

1. During each run of the simulator, additional information that characterizes the subhalo population and lensing process is stored together with the simulated observed image.
2. This information is used to train a neural network to approximate the likelihood ratio function.
3. The neural network output is calibrated, ensuring that errors during training do not lead to wrong inference results.
4. The calibrated network output is then used in either a frequentist or Bayesian setting to perform inference.

In the remainder of this section, we will explain these four steps in detail.

3.1. *Extracting additional information from the simulator*

In a first step, we generate training data by simulating a large number of observed lenses. For each lens, we first draw two parameter points from a proposal distribution, $\vartheta, \vartheta' \sim \pi(\vartheta)$. This proposal distribution should cover the region of interest in the parameter space, but does not have to be identical to the prior in a Bayesian inference setting, which allows us to be agnostic about the inference setup at this stage.

Next, the simulator is run for the parameter point ϑ , generating an observed image $x \sim p(x|\vartheta)$. In addition, we calculate and save two quantities: the joint likelihood ratio

$$r(x, z|\vartheta) = \frac{p(x, z|\vartheta)}{p_{\text{ref}}(x, z)} \quad (18)$$

and the joint score

$$t(x, z|\vartheta) = \nabla_{\vartheta} \log p(x, z|\vartheta). \quad (19)$$

The joint likelihood ratio quantifies how much more or less likely a particular simulation chain including the

latent variables z is for the parameter point ϑ compared to a reference distribution

$$p_{\text{ref}} = \int d\vartheta' \pi(\vartheta') p(x, z|\vartheta'), \quad (20)$$

where we choose the marginal distribution of latent variables and observables corresponding to the proposal distribution $\pi(\vartheta)$. Unlike the distribution for a single reference parameter point, this marginal model has support for every potential outcome of the simulation (Hermans et al. 2019). The joint score is the gradient of the joint log likelihood in model parameter space and quantifies if a particular simulation chain becomes more or less likely under infinitesimal changes of the parameters of interest. Both quantities depend on the latent variables of the simulation chain.

We compute the joint likelihood ratio and joint score with Eq. (17). Conveniently, the first and third line of that equation do not explicitly depend on the parameters of interest ϑ and cancel in the joint likelihood ratio and joint score; the remaining terms can be evaluated with little overhead to the simulation code. We also calculate the joint likelihood ratio $r(x, z|\vartheta')$ and the joint score $t(x, z|\vartheta')$ for the second parameter point ϑ' and store the parameter points ϑ and ϑ' , the simulated image x , as well as the joint likelihood ratios and joint scores.

Our training samples consist of 10^6 images, with parameter points chosen from a uniform range in $0.001 < f_{\text{sub}} < 0.2$ and $-1.5 < \beta < -0.5$.

3.2. Machine learning

How are the joint likelihood ratio and joint score, which are conditional on the latent variables z , useful for inference based on the likelihood function $p(x|\vartheta)$, which only depends on the observed lens images and the parameters of interest? Consider the functional

$$\begin{aligned} L[g(x, \vartheta)] &= \int d\vartheta \int d\vartheta' \int dx \int dz \pi(\vartheta) \pi(\vartheta') p(x, z|\vartheta) \\ &\times \left[-s \log g - (1-s) \log(1-g) - s' \log g' - (1-s') \log(1-g') \right. \\ &\quad \left. + \alpha \left\{ \left| t - \nabla_{\vartheta} \log \frac{1-g}{g} \right|_{\vartheta}^2 + \left| t' - \nabla_{\vartheta} \log \frac{1-g}{g} \right|_{\vartheta'}^2 \right\} \right], \end{aligned} \quad (21)$$

where we have abbreviated $s \equiv s(x, z|\vartheta) \equiv 1/(1 + r(x, z|\vartheta))$, $s' \equiv s(x, z|\vartheta') \equiv 1/(1 + r(x, z|\vartheta'))$, $g \equiv g(x, \vartheta)$, $g' \equiv g(x, \vartheta')$, $t \equiv t(x, z|\vartheta)$, and $t' \equiv t(x, z|\vartheta')$ for readability. Note that the test function $g(x, \vartheta)$ is a function of x and ϑ only. The first two lines are an improved

version of the cross-entropy loss, in which the joint likelihood ratio is used to decrease the variance compared to the canonical cross-entropy (Stoye et al. 2018). The last line adds gradient information, weighted by a hyperparameter α .

As shown in Stoye et al. (2018), this “ALICES” loss functional is minimized by the function

$$g^*(x, \vartheta) \equiv \arg \min_g L[g(x, \vartheta)] = \frac{1}{1 + r(x|\vartheta)}, \quad (22)$$

one-to-one with the likelihood ratio function

$$r(x|\vartheta) \equiv \frac{p(x|\vartheta)}{p_{\text{ref}}(x)} = \frac{1 - g^*(x, \vartheta)}{g^*(x, \vartheta)}. \quad (23)$$

We demonstrate the minimization of this functional explicitly in Appendix A. This means that if we can construct the functional in Eq. (21) with the joint likelihood ratio and joint score extracted from the simulator and numerically minimize it, the resulting function lets us reconstruct the (otherwise intractable) likelihood ratio function $r(x|\vartheta)$! Essentially, this step lets us integrate out the dependence on latent variables z from the joint likelihood ratio and score, but in a general, functional form that does not depend on a set of observed images.

This is why extraction of the joint likelihood ratio and joint score has been described with the analogy of “mining gold” from the simulator (Brehmer et al. 2018c): while calculating these quantities may require some effort and changes to the simulator code, through the minimization of a suitable functional they allow us to calculate the otherwise intractable likelihood ratio function.

In practice, we implement this minimization with machine learning. A neural network plays the role of the test function $g(x, \vartheta)$, the integrals in Eq. (21) are approximated with a sum over training data sampled according to $\pi(\vartheta)\pi(\vartheta')p(x, z|\vartheta)$, and we minimize the loss numerically through a stochastic gradient descent algorithm. The neural network trained in this way provides an estimator $\hat{r}(x|\vartheta)$ of the likelihood ratio function that is exact in the limit of infinite training samples, sufficient network capacity, and efficient minimization. Note the “parameterized” structure of the network, in which a single neural network is trained to estimate the likelihood ratio over all of the parameter space, with the tested parameter point ϑ being an input to the network (Cranmer et al. 2015; Baldi et al. 2016). This approach is more efficient than a point-by-point analysis of a grid of parameter points: it allows the network to “borrow” information from neighboring parameter points, benefiting from the typically smooth structure of the parameter space.

Given the image nature of the lensing data, we choose a convolutional network architecture based on

the ResNet-18 (He et al. 2016) implementation in PyTorch (Paszke et al. 2017). The parameters ϑ enter as additional inputs in the fully connected layers of the network. Compared to the original ResNet-18 architecture, we add another fully connected layer at the end to ensure that the relation between parameters of interest and image data can be modeled. All inputs are normalized to zero mean and unit variance. We train the networks by minimizing the loss in Eq. (21) with $\alpha = 2 \cdot 10^{-3}$ over 100 epochs with a batch size of 128 using stochastic gradient descent with momentum (Qian 1999), exponentially decaying the learning rate from 0.01 to 0.0001 with early stopping. We pretrain the model on data generated from a simplified version of the simulator described in Appendix B. This architecture and hyperparameter configuration performed best during a rough hyperparameter scan, though for this proof-of-concept study we have not performed an exhaustive optimization.

3.3. Calibration

In reality, the neural network might not learn the likelihood ratio function $r(x|\vartheta)$ exactly, for instance due to limited training data or inefficient training. To make sure that our inference results are correct even in this case, we calibrate the network output with histograms (Cranmer et al. 2015; Brehmer et al. 2018b). For every parameter point ϑ that we want to test, we simulate a set of images $\{x\} \sim p(x|\vartheta)$ from this parameter point and calculate the network prediction $\hat{r} \equiv \hat{r}(x|\vartheta)$ for each image. We also simulate a set of images $\{x\} \sim p_{\text{ref}}(x)$ from the reference model, again calculating the network prediction \hat{r} for each lens. The calibrated likelihood ratio is then calculated from histograms of the network predictions as

$$\hat{r}_{\text{cal}}(x|\vartheta) = \frac{\hat{p}(\hat{r}|\vartheta)}{\hat{p}_{\text{ref}}(\hat{r})} \quad (24)$$

where the $\hat{p}(\dots)$ denote probability densities estimated with univariate histograms.

This additional calibration stage comes with a certain computational cost that increases linearly with the number of evaluated parameter points. However, it guarantees that as long as the simulator accurately models the process, the inference results will be perfect or conservative, but not be too optimistic, even if the neural network output is substantially different from the true likelihood ratio. As a compromise, the calibration procedure can be used only at selected parameter points, serving as a cross-check of the fidelity of the network output.

We will show results both without and with calibration. Where calibration is used, it is based on histograms

with 60 bins, with bin boundaries determined automatically to match the distribution of likelihood ratios.

3.4. Inference

After a neural network has been trained (and optionally calibrated) to estimate the likelihood ratio function, it provides the basic ingredient to both frequentist and Bayesian inference. For frequentist hypothesis tests, the likelihood ratio provides the most powerful test statistic (Neyman & Pearson 1933). In addition, its asymptotic properties allow us in many cases to directly translate a value of the likelihood ratio into a p -value and thus into exclusion limits at a given confidence level (Wilks 1938; Wald 1943; Cowan et al. 2011).

For Bayesian inference, note that we can write Bayes' theorem as

$$\begin{aligned} p(\vartheta|\{x_i\}) &= \frac{p(\vartheta) \prod_i p(x_i|\vartheta)}{\int d\vartheta' p(\vartheta') \prod_i p(x_i|\vartheta')} \\ &= p(\vartheta) \left[\int d\vartheta' p(\vartheta') \prod_i \frac{p(x_i|\vartheta')}{p(x_i|\vartheta)} \right]^{-1} \\ &\approx p(\vartheta) \left[\int d\vartheta' p(\vartheta') \prod_i \frac{\hat{r}(x_i|\vartheta')}{\hat{r}(x_i|\vartheta)} \right]^{-1}, \end{aligned} \quad (25)$$

where $\{x_i\}$ is the set of observed lens images and $p(\vartheta)$ is the prior on the parameters of interest, which may be different from the proposal distribution $\pi(\vartheta)$ used during the generation of training data. The posterior can thus be directly calculated given an estimator \hat{r} , provided that the space of the parameters of interest is low-dimensional enough to calculate the integral, or with MCMC or variational inference techniques otherwise.

While our approach to inference is strongly based on the ideas in Brehmer et al. (2018a,b,c); Stoye et al. (2018), there are some novel features in our analysis that we would like to highlight briefly. Unlike in those earlier papers, we use a marginal model based on the proposal distribution $\pi(\vartheta)$ as reference model in the denominator of the likelihood ratio, which substantially improves the numerical stability of the algorithm. This choice also allows us to include the “flipped” terms with s' and g' in the loss function in Eq. (21); we found that this new, improved version of the ALICES loss improves the sample efficiency of our algorithms. Both of these improvements are inspired by Hermans et al. (2019). Finally, this is the first application of the “gold mining” idea to image data, the first combination with a convolutional network architecture, and the first use for Bayesian inference.

4. RESULTS

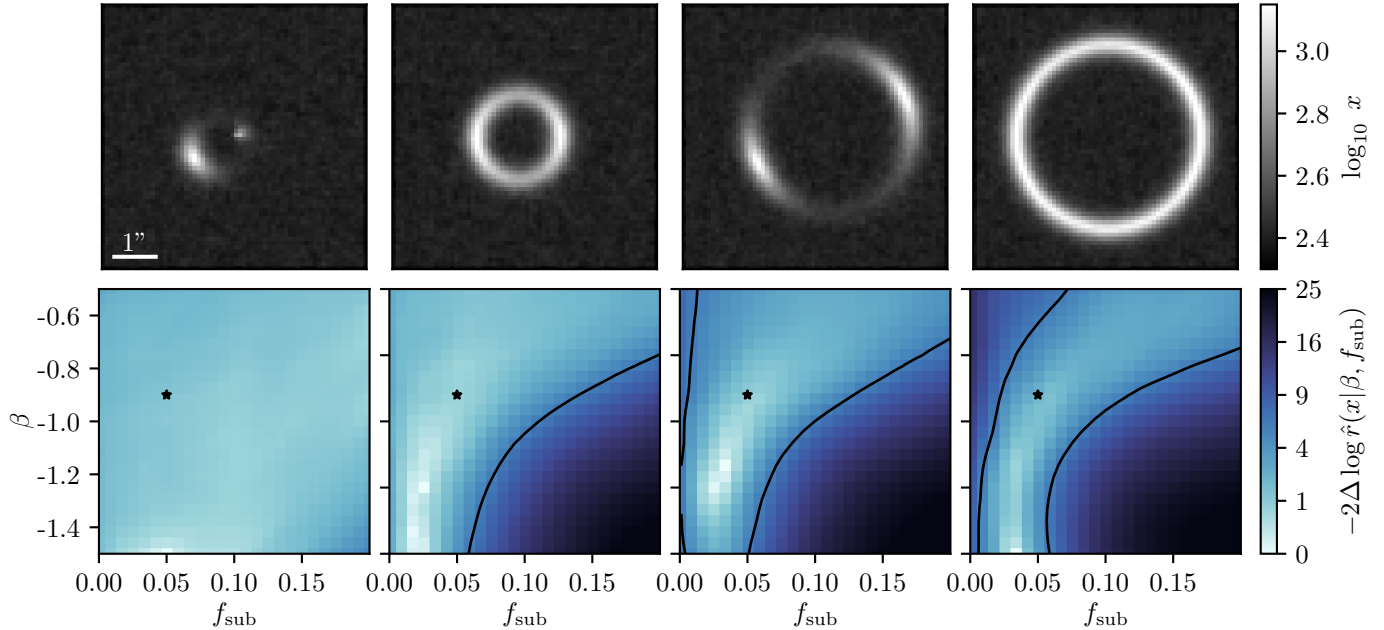


Figure 2. Four simulated lens images (upper panels) and the corresponding likelihood ratio maps estimated by the network (lower panels, without calibration). The star marks the true point used to generate the images, the black line shows 95% CL contours in parameter space based on each image.

After training the neural network using the simulations described in Sec. 2 and the formalism described in Sec. 3, we can run the inference step on a given set of images to extract the likelihood ratio estimates $\hat{r}(x|\vartheta)$ associated with the substructure parameters of interest $\{f_{\text{sub}}, \beta\}$. We start by illustrating in Fig. 2 inference on individual simulated lensed images realizing substructure corresponding to benchmark parameters $\beta = -0.9$ and $f_{\text{sub}} = 0.05$. The top row shows example simulated images, with the corresponding inferred 2-D likelihood surfaces shown in the bottom row. The true parameter point is marked with a star and the 95% confidence level (CL) contours are shown.

Several interesting features can already be seen in these results. The 95% CL contours contain the true parameter point, with the overall likelihood surface being strongly correlated with the corresponding image. A smaller projected surface area of the lensed arc, resulting from a smaller host halo or a larger offset between the host and source centers, generally results in a flatter likelihood surface. This is expected, since a smaller host galaxy will contain relatively less substructure, and a smaller host or larger relative offset will result in a smaller effective arc area over which the substructure can imprint itself. The first column of Fig. 2 shows an example of such a system. In contrast, the last columns show a system with a relatively massive host and a small offset, producing a symmetric image with a larger effective arc surface area over which the effects of substructure

can be discerned. This results in a “peakier” inferred likelihood surface, corresponding to a higher sensitivity to f_{sub} and β . The second and third columns of Fig. 2 correspond to systems with a small, centered and a large, offset halo respectively, and show intermediate sensitivity to substructure properties.

The individual likelihood estimates can be combined in a straightforward manner into a stacked test statistic, yielding a combined analysis of an ensemble of lenses. The expected likelihood surface per-image in the asymptotic limit is shown in the left panel of Fig. 3, with the 1-D slice corresponding to $\beta = -0.9$ shown in the right panel. The 95% CL expected exclusion limits for 5, 20, and 100 lenses are shown using the dotted, dashed, and solid lines respectively. The procedure can easily be extended to an arbitrarily large collection of lenses, providing an unbiased estimate of the underlying substructure properties.

We find that, at least within the simplifying assumptions of our simulator, an analysis of a few tens of lenses is already sensitive to the overall substructure abundance parameterized by f_{sub} . A larger observed lens sample provides a tighter constraint on substructure properties. Approximately 100 lens images are required to begin resolving β . The expected exclusion contours are centered around the true values, confirming that our inference methods yield unbiased results. Note the “banana” shape of the expected exclusion limits, which approximately traces the total deflection contributed by

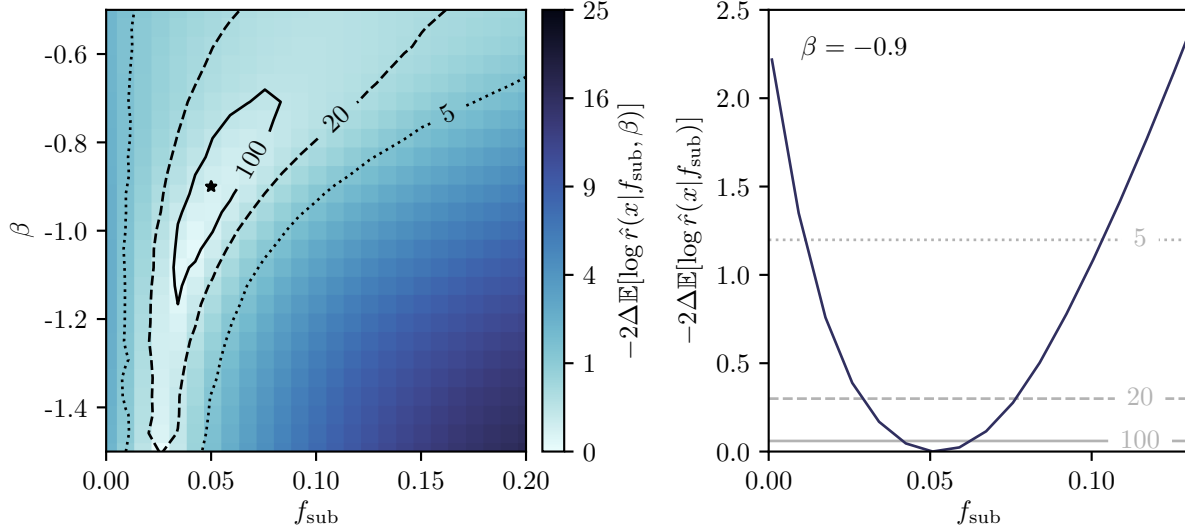


Figure 3. (Left) Expected per-lens likelihood ratio map assuming $\beta = -0.9$ and $f_{\text{sub}} = 0.05$ in the two-dimensional parameter space. The lines show expected 95% CL exclusion limits for 5 (dotted), 20 (dashed), and 100 (solid) observed lenses. While the colormap shows the network output without calibration, the lines include the calibration procedure described in Sec. 3.3. (Right) Expected per-lens likelihood ratio along a one-dimensional slice at $\beta = -0.9$.

substructure. We demonstrate this in Fig. 4, where we show a proxy for the total subhalo-induced deflection,

$$\tilde{\phi}_r = \sum_{\text{subhalos}} 4\kappa_s r_s, \quad (26)$$

equal to the space-independent part of Eq. (11), and compare it to the expected exclusion limits. We note that this comparison is schematic, as the subtle effects of substructure over a wide range of masses (which our method is sensitive to) cannot be quantified through a single number (the total deflection, here).

With the likelihood ratio in hand, a Bayesian interpretation is easily admitted using Eq. (25). In Fig. 5 we show the derived posterior, assuming a Gaussian prior with mean -0.9 and standard deviation 0.1 on the slope β . This choice is intended to capture a prior expectation on the subhalo mass function slope consistent with the Cold Dark Matter scenario (Springel et al. 2008; Madau et al. 2008). As expected from the likelihood maps, we find a posterior density peaked around the true point.

5. EXTENSIONS

For the proof-of-concept analysis presented here our lensing simulation makes a number of simplifying assumptions in order to highlight the broad methodological points in a computationally tractable setting. An application of our method to real lensing data will invariably require modifications to our simulation and inference pipelines to account for the vast physical diversity in host and source galaxy morphologies, as well as ways to deal with more realistic detector response. Modeling

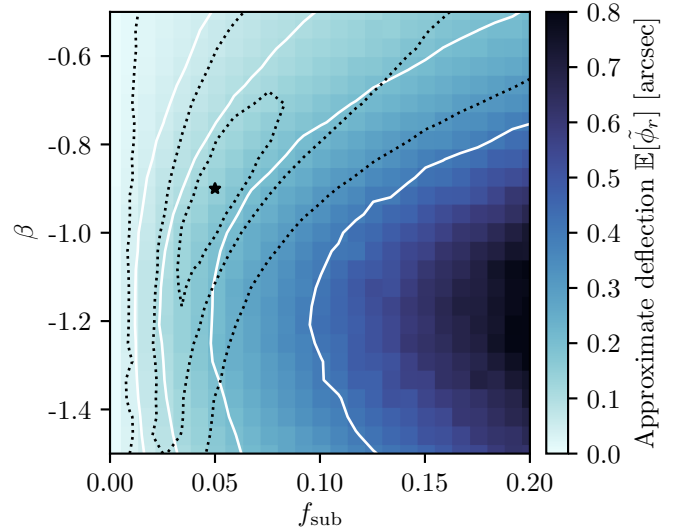


Figure 4. Expected approximate deflection $\tilde{\phi}_r$ as defined in Eq. 26 as a function of f_{sub} and β . The solid white lines show contours of constant $\tilde{\phi}_r$, while the dotted black lines show the expected exclusion limits from the left panel of Fig. 3.

substructure in a more involved setting than presented here (e. g., to account for tidal evolution and/or suppression of small-scale structure), and accounting for substructure along the line of sight is also desired. We will now discuss these features and comment on how they might affect our pipeline and the results presented here, leaving implementation and application to real lensing data to future work.

First, we currently fix all properties of the background source as described in Sec. 2.3. It is straightforward to

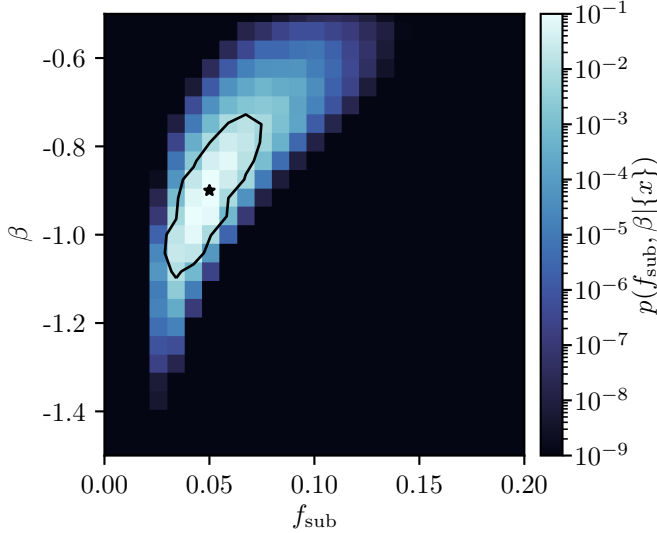


Figure 5. Expected posterior and 95% credible regions for 100 observed lenses. The mock observations are generated for $f_{\text{sub}} = 0.05$ and $\beta = -0.9$. We assume a uniform prior on f_{sub} and a Gaussian prior with mean -0.9 and standard deviation 0.1 for β .

instead draw and marginalize over the parameters associated with a chosen parameterization for the source light distribution, with Gaussian and Sérsic (Sérsic 1963) profile models being common choices. For high-fidelity images (e.g., those obtainable by targeted followups or interferometric imaging) more complicated features in the background galaxies such as outflows and dust-obscured regions may not be adequately captured by such a parameterization and could introduce degeneracies with the effects of substructure. Alternative parameterizations using shapelet basis sets (Birrer & Amara 2018; Birrer et al. 2015), and methods based on regularized linear inversion on grids (Nightingale et al. 2018; Suyu et al. 2006; Warren & Dye 2003) have been introduced as ways to model more complicated source features. For our purposes, generative / data-driven modeling of background galaxies could easily be interfaced with our pipeline to account for the variation in structure of the background source (Morn-ingstar et al. 2019).

Similarly, the host lens (and associated host dark matter halo) model can be made more realistic by relaxing the restriction to spherical host halos and including more complicated profiles than the Singular Isothermal Sphere considered here, drawing and marginalizing over additional host parameters as required. External shear, which models the fact that the local large-scale structure environment of the host galaxy can induce an additional overall deflection field in a preferred direction, can sim-

ilarly be parameterized (Schneider 1997; Keeton et al. 1997) and marginalized over.

A realistic simulator should also model the dynamical evolution of subhalos (Despali & Vegetti 2017). Effects associated with tidal disruption due to the large gradient of the galactic potential towards the center of the host galaxy are expected to deplete the fraction of mass bound in substructures there, leading to a depressed overall subhalo abundance (Han et al. 2016) with profile properties (e.g., concentration (Moliné et al. 2017) and a truncation radius (Baltz et al. 2009)) that depend on the distance from the host center. This could easily be implemented within our framework by drawing 3-D positions for the subhalos from the host center and assigning properties consistent with more involved modeling. Our subhalo mass function in Eq. (14) is independent of the lens redshift, but can easily be extended to include this dependency (Hiroshima et al. 2018; Despali & Vegetti 2017).

All of these effects are straightforward to implement in our setup and only require modifications to the simulation code. The inference algorithm is unaffected; since these extensions do not explicitly depend on the parameters of interest, the likelihood terms associated with them cancel in the calculation of the joint likelihood ratio and the joint score. Nevertheless, these changes affect the final observed image and therefore also the true likelihood function; the variance of the joint likelihood ratio and score could therefore increase, requiring larger training samples before the network converges to the correct likelihood ratio function.

With these extensions, the redshift of the background source and the lens will play a more important role. Since these redshifts can potentially be measured through spectroscopic follow-up observations, it is likely that we can improve the performance of the inference algorithm by using this information. We can treat both the source and lens redshift, potentially with added uncertainty to model measurement noise, as additional observables. The input to the neural networks then consists of the observed lens image, the measured (potentially noisy) redshifts, and the tested parameter point. Except for a simple modification of the network architecture, the inference algorithm remains unchanged.

Including line-of-sight substructure can be somewhat more involved, since it necessitates the introduction of a separate line-of-sight halo mass function (Birrer et al. 2017b; Despali et al. 2018; Gilman et al. 2019; Hsueh et al. 2019). Depending on the specific model (and whether foreground substructure is treated as a nuisance effect or additional signal to be leveraged) its parameters could depend on the parameters of interest, which

would require a modification of the calculation of the joint likelihood ratio and joint score. Structurally this is identical to our current modeling of subhalos within the lens. Since the abundance of foreground substructure is expected to be at most comparable to the substructure within the lensing galaxy (depending on the source redshift), we expect that these additional factors in the joint likelihood ratio and joint score will not slow down the overall simulation significantly, and will not increase the variance of the inference techniques too much while having the potential to improve the overall sensitivity of the analysis to substructure abundance in the Universe.

It is expected that a sample of strong lenses will include image-to-image variations on the exposure (through observation time), sky background and detector effects like the points spread function (PSF) depending on the specific scanning strategy of the observatory. The sky background can be marginalized over as usual. Rather than treating the exposure and PSF model as nuisance parameters, passing them as additional *a priori* known inputs to the network in addition to normalizing the network input to unit exposure is likely to improve performance. Multiple color bands can easily be modeled and included as inputs to the neural network as different color channels, something that is commonly done when using the ResNet architecture we consider. This can substantially improve discrimination between light from the source, host, and sky background which tend to have a degree of separation in color space.

While including these extensions in our simulation and inference code is feasible, the detailed modeling is beyond the scope of the current paper. We leave the implementation of these features and application to real lensing data to future work.

6. CONCLUSIONS


Strong lensing offers a unique way to probe the properties and distribution of dark matter on sub-galactic scales through the subtle imprint of substructure on lensed arcs. The high dimensionality of the underlying latent space characterizing substructure poses a significant challenge, however. In this paper, we have introduced a novel simulation-based technique based on the ideas introduced in Brehmer et al. (2018a,b,c); Stoye et al. (2018) for inferring high-level population properties characterizing the distribution of substructure in an ensemble of galaxy-galaxy strong lenses and demonstrated its feasibility through proof-of-principle examples.

Our results on simulated data demonstrate that this method (based on calibrated likelihood ratio estimators with a machine learning back end) offers a promis-

ing way to analyze extended-arc strong lensing images with the goal of inferring properties of dark matter substructure. Our proposed method offers several combined advantages over established techniques. In probing the collective effect of a large number of low-mass, sub-threshold subhalos it can offer sensitivity to the faint end of the subhalo mass function where deviations from the concordance Λ CDM paradigm are most likely to be expressed. It can naturally be applied to perform fast, principled, and concurrent analyses of a large sample of strong lenses that share a common set of hyperparameters describing the underlying substructure population properties. Furthermore, rigorous selection of lensing images out of a large sample is not necessary within our framework since images with a smaller effective arc area or low overall fidelity simply do not contribute significantly to the combined substructure analysis, and non-detections are just as valuable as detections. Finally, our analysis is performed at the level of image data, without incurring loss of information associated with dimensionality reduction.

Although we have focused on a simple proof-of-principle example in this paper, extensions to more realistic scenarios—including more complicated descriptions of the host, source, and substructure populations—are easily admitted within our framework. The flexibility of the proposed method allows for applications beyond substructure population inference. For example, a large lens sample can be used to perform cosmological parameter estimation while accounting for substructure effects and in particular to independently constrain the Hubble constant (Wong et al. 2019; Chen et al. 2019) through its dependence on the angular diameter distance scales in lensing systems.

In conclusion, we suggest a powerful new machine learning-based method to characterize the properties of dark matter substructure within strong lensing galaxies and in the Universe at large. The introduction of our method coincides with the dawn of a new area in observational cosmology, when ongoing and upcoming surveys—e.g., DES, LSST, *Euclid*, and WFIRST—are expected to observe and deliver images of thousands of strong lensing systems which will contain the subtle imprint of dark matter substructure and, potentially, signatures of new physics.

The code used to obtain the results in this study is available at <https://github.com/smsharma/StrongLensing-Inference> .

We thank Simon Birrer, Christopher Fassnacht, Daniel Gilman, Siavash Golkar, and Neal Weiner for useful conversations. JB and KC are partially supported

by NSF awards ACI-1450310, OAC-1836650, and OAC-1841471, and the Moore-Sloan data science environment at NYU. SM is partially supported by the NSF CAREER grant PHY-1554858 and NSF grant PHY-1620727. KC is also supported through the NSF grant PHY-1505463. This work was also supported through the NYU IT High Performance Computing resources, services, and staff expertise. This research has made use of NASA’s Astrophysics Data System.

Software: *Astropy* (Astropy Collaboration et al. 2013, 2018), *Jupyter* (Kluyver et al. 2016), *IPython* (Perez & Granger 2007), *LensPop* (Collett 2015), *MadMiner* (Brehmer et al. 2019), *matplotlib* (Hunter 2007), *NumPy* (van der Walt et al. 2011), *PyTorch* (Paszke et al. 2017), *SciPy* (Jones et al. 2001–).

APPENDIX

A. MINIMUM OF THE LOSS FUNCTIONAL

A central step in our inference technique is numerically minimizing the functional $L[g(x, \vartheta)]$ given in Eq. (21) to obtain an estimator for the likelihood ratio function. Here we will use calculus of variation to explicitly show that the solution given in Eq. (22) in fact minimizes this loss, closely following Brehmer et al. (2018b); Stoye et al. (2018).

First consider the case of $\alpha = 0$, i.e. the functional

$$\begin{aligned} L[g(x, \vartheta)] &= \int d\vartheta \int dx \int dz \pi(\vartheta) \pi(\vartheta') p(x, z|\vartheta) \left(-s \log g - (1-s) \log(1-g) - s' \log g' - (1-s') \log(1-g') \right) \\ &= \int d\vartheta \int dx \underbrace{\left[\int dz \pi(\vartheta) \left(p(x, z|\vartheta) + p_{\text{ref}}(x, z) \right) \left(-s \log g - (1-s) \log(1-g) \right) \right]}_{\equiv F(x, \vartheta)}, \end{aligned} \quad (\text{A1})$$

where we use the shorthand notation $s \equiv s(x, z|\vartheta) \equiv 1/(1+r(x, z|\vartheta))$, $s' \equiv s(x, z|\vartheta') \equiv 1/(1+r(x, z|\vartheta'))$, $g \equiv g(x, \vartheta)$, $g' \equiv g(x, \vartheta')$. The function $g^*(x|\vartheta)$ that minimizes this functional has to satisfy

$$0 \stackrel{!}{=} \left. \frac{\delta F}{\delta g} \right|_{g^*} = \int dz \pi(\vartheta) \left(p(x, z|\vartheta) + p_{\text{ref}}(x, z) \right) \left(-\frac{s}{g^*} + \frac{1-s}{1-g^*} \right) \quad (\text{A2})$$

As long as $\pi(\vartheta) > 0$, this is equivalent to

$$(1-g^*) \int dz \left(p(x, z|\vartheta) + p_{\text{ref}}(x, z) \right) s = g^* \int dz \left(p(x, z|\vartheta) + p_{\text{ref}}(x, z) \right) (1-s) \quad (\text{A3})$$

and finally

$$\begin{aligned} g^*(x|\vartheta) &= \frac{\int dz \left(p(x, z|\vartheta) + p_{\text{ref}}(x, z) \right) s(x, z|\vartheta)}{\int dz \left(p(x, z|\vartheta) + p_{\text{ref}}(x, z) \right)} \\ &= \frac{\int dz \left(p(x, z|\vartheta) + p_{\text{ref}}(x, z) \right) \frac{1}{1+p(x, z|\vartheta)/p_{\text{ref}}(x, z)}}{\int dz \left(p(x, z|\vartheta) + p_{\text{ref}}(x, z) \right)} \\ &= \frac{p_{\text{ref}}(x)}{p(x|\vartheta) + p_{\text{ref}}(x)} = \frac{1}{1+r(x|\vartheta)}, \end{aligned} \quad (\text{A4})$$

in agreement with Eq. (22). Note that this result is independent of the choice of $\pi(\vartheta)$, as long as this proposal distribution has support at all relevant parameter points.

Similarly it can be shown that the gradient term in the loss functional weighted by α is minimized when the gradient of the log likelihood ratio estimated by the neural network is equal to the true score,

$$\nabla_{\vartheta} \log \hat{r}(x|\vartheta) \equiv \nabla_{\vartheta} \log \frac{1-g^*(x, \vartheta)}{g^*(x, \vartheta)} = \nabla_{\vartheta} \log r(x|\vartheta). \quad (\text{A5})$$

We refer the reader to Brehmer et al. (2018b) for the derivation. While not strictly necessary for the inference technique, including this term in the loss function substantially improves the sample efficiency of the algorithm, similar to how gradient information makes any fit converge faster.

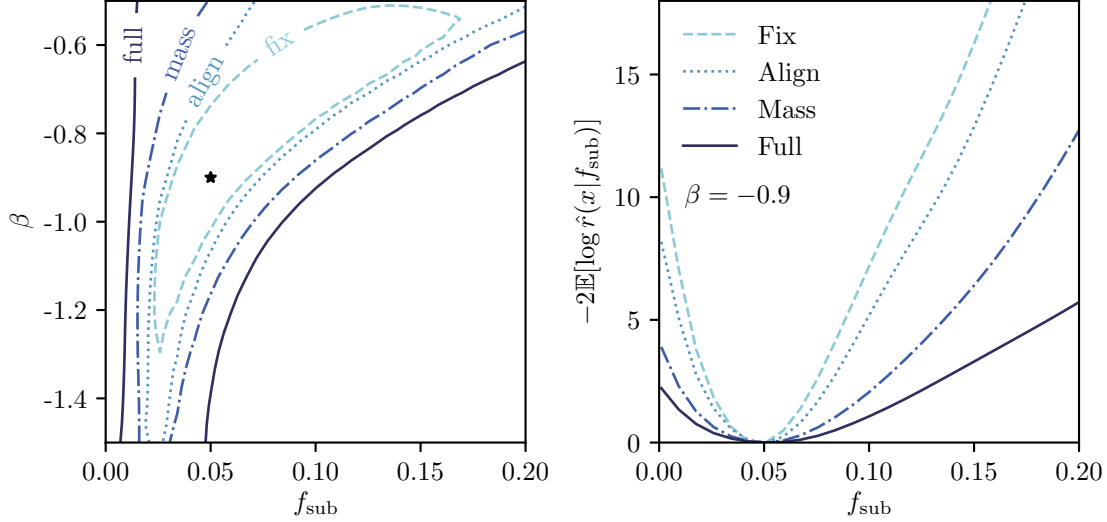


Figure 6. Left: Expected 95% CL exclusion limits for 5 observed lenses for four different levels of complexity of the simulator. Right: expected likelihood ratio along a one-dimensional slice through the parameter space at $\beta = -0.9$ for the same four simulator scenarios. In both panels we compare the “full” simulator discussed in Sec. 2, a scenario in which the host mass is varied but the offset relative to the source is fixed at zero (“mass”), a case in which the source offset is varied but the host halo mass is fixed (“align”), and a toy scenario in which both the offset and the mass of the host halo are fixed (“fix”). The data was generated for $\beta = -0.9$ and $f_{\text{sub}} = 0.05$.

B. SIMPLIFIED SCENARIOS

In order to validate our setup and to disentangle the impact of different latent variables on the inference results we consider three additional versions of our simulation. In the simplest one, which we call “fix”, all source and host properties are fixed to particular value, including the host halo mass and the offset between source and lens, which is set to zero. In the “align” scenario we relax the restriction on the source offset variables θ_x and θ_y and draw them from a Gaussian as described in Sec. 2. In the “mass” version, on the other hand, the offset is fixed at zero, but the host halo mass is drawn from a distribution as described above. We train separate neural networks on lens images generated in these three scenarios and calculated likelihood maps as described in Sec. 3, although to save computation time we do not perform a calibration procedure.

The expected confidence limits for 5 observed lens images in the three simplified scenarios and our “full” setup are compared in Fig. 6. As expected, the more latent variables we keep fixed, the more the inference technique becomes more sensitive to the parameters of interest. In particular fixing the source-host alignment substantially increases the strength of the expected limits.

REFERENCES

- Aaboud, M., Aad, G., Abbott, B., et al. 2019, *Journal of High Energy Physics*, 2019, 142, arXiv: [1903.01400](#), doi: [10.1007/JHEP05\(2019\)142](#)
- Agrawal, P., Cyr-Racine, F.-Y., Randall, L., & Scholtz, J. 2017, *JCAP*, 2017, 021, arXiv: [1702.05482](#), doi: [10.1088/1475-7516/2017/08/021](#)
- Agrawal, P., & Randall, L. 2017, *JCAP*, 2017, 019, arXiv: [1706.04195](#), doi: [10.1088/1475-7516/2017/12/019](#)
- Akerib, D. S., Alsum, S., Araújo, H. M., et al. 2017, *PhRvL*, 118, 021303, arXiv: [1608.07648](#), doi: [10.1103/PhysRevLett.118.021303](#)
- Albert, A., Anderson, B., Bechtol, K., et al. 2017, *ApJ*, 834, 110, arXiv: [1611.03184](#), doi: [10.3847/1538-4357/834/2/110](#)
- Alsing, J., Charnock, T., Feeney, S., & Wandelt, B. 2019, *Monthly Notices of the Royal Astronomical Society*, 488, 4440, arXiv: [1903.00007](#), doi: [10.1093/mnras/stz1960](#)
- Aprile, E., Aalbers, J., Agostini, F., et al. 2018, *PhRvL*, 121, 111302, arXiv: [1805.12562](#), doi: [10.1103/PhysRevLett.121.111302](#)
- Astropy Collaboration, Robitaille, T. P., Tollerud, E. J., et al. 2013, *A&A*, 558, A33, arXiv: [1307.6212](#), doi: [10.1051/0004-6361/201322068](#)

- Astropy Collaboration, Price-Whelan, A. M., Sipőcz, B. M., et al. 2018, *AJ*, 156, 123, arXiv: [1801.02634](#), doi: [10.3847/1538-3881/aabc4f](#)
- Baldi, P., Cranmer, K., Faucett, T., Sadowski, P., & Whiteson, D. 2016, *European Physical Journal C*, 76, 235, arXiv: [1601.07913](#), doi: [10.1140/epjc/s10052-016-4099-4](#)
- Baltz, E. A., Marshall, P., & Oguri, M. 2009, *Journal of Cosmology and Astro-Particle Physics*, 2009, 015, arXiv: [0705.0682](#), doi: [10.1088/1475-7516/2009/01/015](#)
- Bechtol, K., Drlica-Wagner, A., Balbinot, E., et al. 2015, *ApJ*, 807, 50, arXiv: [1503.02584](#), doi: [10.1088/0004-637X/807/1/50](#)
- Birrer, S., & Amara, A. 2018, *Physics of the Dark Universe*, 22, 189, arXiv: [1803.09746](#), doi: [10.1016/j.dark.2018.11.002](#)
- Birrer, S., Amara, A., & Refregier, A. 2015, *The Astrophysical Journal*, 813, 102, arXiv: [1504.07629](#), doi: [10.1088/0004-637X/813/2/102](#)
- . 2017a, *JCAP*, 2017, 037, arXiv: [1702.00009](#), doi: [10.1088/1475-7516/2017/05/037](#)
- Birrer, S., Welschen, C., Amara, A., & Refregier, A. 2017b, *Journal of Cosmology and Astro-Particle Physics*, 2017, 049, arXiv: [1610.01599](#), doi: [10.1088/1475-7516/2017/04/049](#)
- Bode, P., Ostriker, J. P., & Turok, N. 2001, *ApJ*, 556, 93, arXiv: [astro-ph/0010389](#), doi: [10.1086/321541](#)
- Bonaca, A., & Hogg, D. W. 2018, *ApJ*, 867, 101, arXiv: [1804.06854](#), doi: [10.3847/1538-4357/aae4da](#)
- Bonaca, A., Hogg, D. W., Price-Whelan, A. M., & Conroy, C. 2019, *ApJ*, 880, 38, arXiv: [1811.03631](#), doi: [10.3847/1538-4357/ab2873](#)
- Bond, J. R., & Szalay, A. S. 1983, *ApJ*, 274, 443, doi: [10.1086/161460](#)
- Boyanovsky, D., de Vega, H. J., & Sanchez, N. G. 2008, *PhRvD*, 78, 063546, arXiv: [0807.0622](#), doi: [10.1103/PhysRevD.78.063546](#)
- Boyanovsky, D., & Wu, J. 2011, *PhRvD*, 83, 043524, arXiv: [1008.0992](#), doi: [10.1103/PhysRevD.83.043524](#)
- Brehmer, J., Cranmer, K., Louppe, G., & Pavez, J. 2018a, *PhRvL*, 121, 111801, arXiv: [1805.00013](#), doi: [10.1103/PhysRevLett.121.111801](#)
- . 2018b, *PhRvD*, 98, 052004, arXiv: [1805.00020](#), doi: [10.1103/PhysRevD.98.052004](#)
- Brehmer, J., Kling, F., Espejo, I., & Cranmer, K. 2019, arXiv e-prints, arXiv:1907.10621, arXiv: [1907.10621](#)
- Brehmer, J., Louppe, G., Pavez, J., & Cranmer, K. 2018c, arXiv e-prints, arXiv:1805.12244, arXiv: [1805.12244](#)
- Brennan, S., Benson, A. J., Cyr-Racine, F.-Y., et al. 2019, *Monthly Notices of the Royal Astronomical Society*, 488, 5085, doi: [10.1093/mnras/stz1607](#)
- Brewer, B. J., Huijser, D., & Lewis, G. F. 2016, *MNRAS*, 455, 1819, arXiv: [1508.00662](#), doi: [10.1093/mnras/stv2370](#)
- Brooks, A. M. 2018, arXiv e-prints, arXiv:1812.00044, arXiv: [1812.00044](#)
- Buckley, M. R., & DiFranzo, A. 2018, *PhRvL*, 120, 051102, arXiv: [1707.03829](#), doi: [10.1103/PhysRevLett.120.051102](#)
- Buckley, M. R., & Peter, A. H. G. 2018, *Physics Reports*, 761, 1, arXiv: [1712.06615](#), doi: [10.1016/j.physrep.2018.07.003](#)
- Buschmann, M., Kopp, J., Safdi, B. R., & Wu, C.-L. 2018, *PhRvL*, 120, 211101, arXiv: [1711.03554](#), doi: [10.1103/PhysRevLett.120.211101](#)
- Carlberg, R. G. 2012, *ApJ*, 748, 20, arXiv: [1109.6022](#), doi: [10.1088/0004-637X/748/1/20](#)
- Carlberg, R. G., & Grillmair, C. J. 2013, *ApJ*, 768, 171, arXiv: [1303.4342](#), doi: [10.1088/0004-637X/768/2/171](#)
- Chang, L. J., Lisanti, M., & Mishra-Sharma, S. 2018, *PhRvD*, 98, 123004, arXiv: [1804.04132](#), doi: [10.1103/PhysRevD.98.123004](#)
- Chatterjee, S., & Koopmans, L. V. E. 2018, *MNRAS*, 474, 1762, arXiv: [1710.03075](#), doi: [10.1093/mnras/stx2674](#)
- Chen, G. C. F., Fassnacht, C. D., Suyu, S. H., et al. 2019, arXiv e-prints, arXiv:1907.02533, arXiv: [1907.02533](#)
- Chen, R. T. Q., Rubanova, Y., Bettencourt, J., & Duvenaud, D. 2018, arXiv e-prints, arXiv:1806.07366, arXiv: [1806.07366](#)
- Ciotti, L., & Bertin, G. 1999, *A&A*, 352, 447
- Collett, T. E. 2015, *ApJ*, 811, 20, arXiv: [1507.02657](#), doi: [10.1088/0004-637X/811/1/20](#)
- Cowan, G., Cranmer, K., Gross, E., & Vitells, O. 2011, *European Physical Journal C*, 71, 1554, arXiv: [1007.1727](#), doi: [10.1140/epjc/s10052-011-1554-0](#)
- Cranmer, K., Pavez, J., & Louppe, G. 2015, arXiv e-prints, arXiv:1506.02169, arXiv: [1506.02169](#)
- Cui, X., Abdukerim, A., Chen, W., et al. 2017, *PhRvL*, 119, 181302, doi: [10.1103/PhysRevLett.119.181302](#)
- Cyr-Racine, F.-Y., Keeton, C. R., & Moustakas, L. A. 2019, *PhRvD*, 100, 023013, arXiv: [1806.07897](#), doi: [10.1103/PhysRevD.100.023013](#)
- Cyr-Racine, F.-Y., Moustakas, L. A., Keeton, C. R., Sigurdson, K., & Gilman, D. A. 2016, *PhRvD*, 94, 043505, arXiv: [1506.01724](#), doi: [10.1103/PhysRevD.94.043505](#)
- Dalal, N., & Kochanek, C. S. 2002, *ApJ*, 572, 25, arXiv: [astro-ph/0111456](#), doi: [10.1086/340303](#)
- Dalcanton, J. J., & Hogan, C. J. 2001, *ApJ*, 561, 35, arXiv: [astro-ph/0004381](#), doi: [10.1086/323207](#)

- Dark Energy Survey Collaboration, Abbott, T., Abdalla, F. B., et al. 2016, *Monthly Notices of the Royal Astronomical Society*, 460, 1270, arXiv: [1601.00329](#), doi: [10.1093/mnras/stw641](#)
- Daylan, T., Cyr-Racine, F.-Y., Diaz Rivero, A., Dvorkin, C., & Finkbeiner, D. P. 2018, *ApJ*, 854, 141, arXiv: [1706.06111](#), doi: [10.3847/1538-4357/aaaa1e](#)
- Despali, G., & Vegetti, S. 2017, *MNRAS*, 469, 1997, arXiv: [1608.06938](#), doi: [10.1093/mnras/stx966](#)
- Despali, G., Vegetti, S., White, S. D. M., Giocoli, C., & van den Bosch, F. C. 2018, *Monthly Notices of the Royal Astronomical Society*, 475, 5424, arXiv: [1710.05029](#), doi: [10.1093/mnras/sty159](#)
- Diaz Rivero, A., Cyr-Racine, F.-Y., & Dvorkin, C. 2018, *PhRvD*, 97, 023001, arXiv: [1707.04590](#), doi: [10.1103/PhysRevD.97.023001](#)
- Díaz Rivero, A., Dvorkin, C., Cyr-Racine, F.-Y., Zavala, J., & Vogelsberger, M. 2018, *PhRvD*, 98, 103517, arXiv: [1809.00004](#), doi: [10.1103/PhysRevD.98.103517](#)
- Dinev, T., & Gutmann, M. U. 2018, arXiv e-prints, arXiv:1810.09899, arXiv: [1810.09899](#)
- Dinh, L., Krueger, D., & Bengio, Y. 2014, ArXiv e-prints, arXiv: [1410.8516](#)
- Dinh, L., Sohl-Dickstein, J., & Bengio, S. 2016, ArXiv e-prints, arXiv: [1605.08803](#)
- Drlica-Wagner, A., Mao, Y.-Y., Adhikari, S., et al. 2019, arXiv e-prints, arXiv:1902.01055, arXiv: [1902.01055](#)
- Efstathiou, G. 1992, *MNRAS*, 256, 43P, doi: [10.1093/mnras/256.1.43P](#)
- Errani, R., Peñarrubia, J., Laporte, C. F. P., & Gómez, F. A. 2017, *MNRAS*, 465, L59, arXiv: [1608.01849](#), doi: [10.1093/mnras/slz211](#)
- Fan, J., Katz, A., Randall, L., & Reece, M. 2013, *Physics of the Dark Universe*, 2, 139, arXiv: [1303.1521](#), doi: [10.1016/j.dark.2013.07.001](#)
- Fan, Y., Nott, D. J., & Sisson, S. A. 2012, ArXiv e-prints, arXiv: [1212.1479](#)
- Fitts, A., Boylan-Kolchin, M., Elbert, O. D., et al. 2017, *MNRAS*, 471, 3547, arXiv: [1611.02281](#), doi: [10.1093/mnras/stx1757](#)
- Fitts, A., Boylan-Kolchin, M., Bozek, B., et al. 2018, arXiv e-prints, arXiv:1811.11791, arXiv: [1811.11791](#)
- Garrison-Kimmel, S., Wetzel, A., Bullock, J. S., et al. 2017, *MNRAS*, 471, 1709, arXiv: [1701.03792](#), doi: [10.1093/mnras/stx1710](#)
- Germain, M., Gregor, K., Murray, I., & Larochelle, H. 2015, ArXiv e-prints, arXiv: [1502.03509](#)
- Gilman, D., Birrer, S., Treu, T., Keeton, C. R., & Nierenberg, A. 2018, *Monthly Notices of the Royal Astronomical Society*, 481, 819, arXiv: [1712.04945](#), doi: [10.1093/mnras/sty2261](#)
- Gilman, D., Birrer, S., Treu, T., Nierenberg, A., & Benson, A. 2019, *Monthly Notices of the Royal Astronomical Society*, 1618, arXiv: [1901.11031](#), doi: [10.1093/mnras/stz1593](#)
- Grathwohl, W., Chen, R. T. Q., Bettencourt, J., Sutskever, I., & Duvenaud, D. 2018, ArXiv e-prints, arXiv: [1810.01367](#)
- Gutmann, M. U., Dutta, R., Kaski, S., & Corander, J. 2017, *Statistics and Computing*, 1
- Han, J., Cole, S., Frenk, C. S., & Jing, Y. 2016, *Monthly Notices of the Royal Astronomical Society*, 457, 1208, arXiv: [1509.02175](#), doi: [10.1093/mnras/stv2900](#)
- He, K., Zhang, X., Ren, S., & Sun, J. 2016, in *Proceedings of the IEEE conference on computer vision and pattern recognition*, 770–778
- Hermans, J., Begy, V., & Louppe, G. 2019, arXiv e-prints, arXiv:1903.04057, arXiv: [1903.04057](#)
- Hezaveh, Y., Dalal, N., Holder, G., et al. 2016a, *JCAP*, 2016, 048, arXiv: [1403.2720](#), doi: [10.1088/1475-7516/2016/11/048](#)
- Hezaveh, Y. D., Dalal, N., Marrone, D. P., et al. 2016b, *ApJ*, 823, 37, arXiv: [1601.01388](#), doi: [10.3847/0004-637X/823/1/37](#)
- Hiroshima, N., Ando, S., & Ishiyama, T. 2018, *Physical Review D*, 97, 123002, arXiv: [1803.07691](#), doi: [10.1103/PhysRevD.97.123002](#)
- Hsueh, J.-W., Enzi, W., Vegetti, S., et al. 2019, arXiv e-prints, arXiv:1905.04182, arXiv: [1905.04182](#)
- Huang, C.-W., Krueger, D., Lacoste, A., & Courville, A. 2018, ArXiv e-prints, arXiv: [1804.00779](#)
- Hunter, J. D. 2007, *Computing In Science & Engineering*, 9, 90
- Jimenez Rezende, D., & Mohamed, S. 2015, ArXiv e-prints, arXiv: [1505.05770](#)
- Johnston, K. V., Zhao, H., Spergel, D. N., & Hernquist, L. 1999, *ApJL*, 512, L109, arXiv: [astro-ph/9807243](#), doi: [10.1086/311876](#)
- Jones, E., Oliphant, T., Peterson, P., et al. 2001–, *SciPy: Open source scientific tools for Python*. <http://www.scipy.org/>
- Kahlhoefer, F., Kaplinghat, M., Slatyer, T. R., & Wu, C.-L. 2019, arXiv e-prints, arXiv:1904.10539, arXiv: [1904.10539](#)
- Kaplinghat, M., Keeley, R. E., Linden, T., & Yu, H.-B. 2014, *PhRvL*, 113, 021302, arXiv: [1311.6524](#), doi: [10.1103/PhysRevLett.113.021302](#)

- Kaplinghat, M., Tulin, S., & Yu, H.-B. 2016, *PhRvL*, 116, 041302, arXiv: [1508.03339](#), doi: [10.1103/PhysRevLett.116.041302](#)
- Keeton, C. R. 2001, arXiv e-prints, astro, arXiv: [astro-ph/0102341](#)
- Keeton, C. R., Kochanek, C. S., & Seljak, U. 1997, *The Astrophysical Journal*, 482, 604, arXiv: [astro-ph/9610163](#), doi: [10.1086/304172](#)
- Kingma, D. P., & Dhariwal, P. 2018, arXiv e-prints, arXiv:1807.03039, arXiv: [1807.03039](#)
- Kluyver, T., Ragan-Kelley, B., Pérez, F., et al. 2016, in *ELPUB*
- Koposov, S., Belokurov, V., Evans, N. W., et al. 2008, *ApJ*, 686, 279, arXiv: [0706.2687](#), doi: [10.1086/589911](#)
- Koposov, S. E., Belokurov, V., Torrealba, G., & Evans, N. W. 2015, *ApJ*, 805, 130, arXiv: [1503.02079](#), doi: [10.1088/0004-637X/805/2/130](#)
- Lisanti, M., Mishra-Sharma, S., Rodd, N. L., & Safdi, B. R. 2018, *PhRvL*, 120, 101101, arXiv: [1708.09385](#), doi: [10.1103/PhysRevLett.120.101101](#)
- Louppe, G., & Cranmer, K. 2017, ArXiv e-prints, arXiv: [1707.07113](#)
- LSST Science Collaboration, Abell, P. A., Allison, J., et al. 2009, arXiv e-prints, arXiv:0912.0201, arXiv: [0912.0201](#)
- Lueckmann, J.-M., Bassetto, G., Karaletsos, T., & Macke, J. H. 2018, arXiv e-prints, arXiv:1805.09294, arXiv: [1805.09294](#)
- Lueckmann, J.-M., Goncalves, P. J., Bassetto, G., et al. 2017, arXiv e-prints, arXiv:1711.01861, arXiv: [1711.01861](#)
- Madau, P., Diemand, J., & Kuhlen, M. 2008, *The Astrophysical Journal*, 679, 1260, arXiv: [0802.2265](#), doi: [10.1086/587545](#)
- Moliné, Á., Sánchez-Conde, M. A., Palomares-Ruiz, S., & Prada, F. 2017, *Monthly Notices of the Royal Astronomical Society*, 466, 4974, arXiv: [1603.04057](#), doi: [10.1093/mnras/stx026](#)
- Morningstar, W. R., Perreault Levasseur, L., Hezaveh, Y. D., et al. 2019, arXiv e-prints, arXiv:1901.01359, arXiv: [1901.01359](#)
- Nadler, E. O., Mao, Y.-Y., Green, G. M., & Wechsler, R. H. 2019, *The Astrophysical Journal*, 873, 34, arXiv: [1809.05542](#), doi: [10.3847/1538-4357/ab040e](#)
- Navarro, J. F., Frenk, C. S., & White, S. D. M. 1996, *ApJ*, 462, 563, doi: [10.1086/177173](#)
- . 1997, *ApJ*, 490, 493, doi: [10.1086/304888](#)
- Neyman, J., & Pearson, E. S. 1933, *Philosophical Transactions of the Royal Society of London Series A*, 231, 289, doi: [10.1098/rsta.1933.0009](#)
- Nightingale, J. W., Dye, S., & Massey, R. J. 2018, *Monthly Notices of the Royal Astronomical Society*, 478, 4738, arXiv: [1708.07377](#), doi: [10.1093/mnras/sty1264](#)
- Oguri, M., & Marshall, P. J. 2010, *Monthly Notices of the Royal Astronomical Society*, 405, 2579, arXiv: [1001.2037](#), doi: [10.1111/j.1365-2966.2010.16639.x](#)
- Paige, B., & Wood, F. 2016, ArXiv e-prints, arXiv: [1602.06701](#)
- Papamakarios, G., & Murray, I. 2016, in *Advances in Neural Information Processing Systems*, 1028–1036
- Papamakarios, G., Pavlakou, T., & Murray, I. 2017, ArXiv e-prints, arXiv: [1705.07057](#)
- Papamakarios, G., Sterratt, D. C., & Murray, I. 2018, ArXiv e-prints, arXiv: [1805.07226](#)
- Paszke, A., Gross, S., Chintala, S., et al. 2017, in *NIPS-W*
- Perez, F., & Granger, B. E. 2007, *Computing in Science and Engineering*, 9, 21, doi: [10.1109/MCSE.2007.53](#)
- Peter, A. H. G., Rocha, M., Bullock, J. S., & Kaplinghat, M. 2013, *MNRAS*, 430, 105, arXiv: [1208.3026](#), doi: [10.1093/mnras/sts535](#)
- Planck Collaboration, Ade, P. A. R., Aghanim, N., et al. 2016, *Astronomy and Astrophysics*, 594, A13, arXiv: [1502.01589](#), doi: [10.1051/0004-6361/201525830](#)
- Qian, N. 1999, *Neural Netw.*, 12, 145, doi: [10.1016/S0893-6080\(98\)00116-6](#)
- Read, J. I., Iorio, G., Agertz, O., & Fraternali, F. 2017, *MNRAS*, 467, 2019, arXiv: [1607.03127](#), doi: [10.1093/mnras/stx147](#)
- Refregier, A., Amara, A., Kitching, T. D., et al. 2010, arXiv e-prints, arXiv:1001.0061, arXiv: [1001.0061](#)
- Rubin, D. B. 1984, *Ann. Statist.*, 12, 1151, doi: [10.1214/aos/1176346785](#)
- Sánchez-Conde, M. A., & Prada, F. 2014, *MNRAS*, 442, 2271, arXiv: [1312.1729](#), doi: [10.1093/mnras/stu1014](#)
- Schneider, P. 1997, *Monthly Notices of the Royal Astronomical Society*, 292, 673, arXiv: [astro-ph/9706185](#), doi: [10.1093/mnras/292.3.673](#)
- Schneider, P., Ehlers, J., & Falco, E. E. 1992, *Gravitational Lenses*, doi: [10.1007/978-3-662-03758-4](#)
- Sérsic, J. L. 1963, *Boletín de la Asociación Argentina de Astronomía La Plata Argentina*, 6, 41
- Sirunyan, A. M., Tumasyan, A., Adam, W., et al. 2017, *Physics Letters B*, 769, 520, arXiv: [1611.03568](#), doi: [10.1016/j.physletb.2017.02.012](#)
- Springel, V., Wang, J., Vogelsberger, M., et al. 2008, *Monthly Notices of the Royal Astronomical Society*, 391, 1685, arXiv: [0809.0898](#), doi: [10.1111/j.1365-2966.2008.14066.x](#)

- Stoye, M., Brehmer, J., Louppe, G., Pavez, J., & Cranmer, K. 2018, arXiv e-prints, arXiv:1808.00973, arXiv: [1808.00973](#)
- Suyu, S. H., Marshall, P. J., Hobson, M. P., & Blandford, R. D. 2006, Monthly Notices of the Royal Astronomical Society, 371, 983, arXiv: [astro-ph/0601493](#), doi: [10.1111/j.1365-2966.2006.10733.x](#)
- Thomas, O., Dutta, R., Corander, J., Kaski, S., & Gutmann, M. U. 2016, arXiv e-prints, arXiv:1611.10242, arXiv: [1611.10242](#)
- Tran, D., Ranganath, R., & Blei, D. 2017, in Advances in Neural Information Processing Systems 30, ed. I. Guyon, U. V. Luxburg, S. Bengio, H. Wallach, R. Fergus, S. Vishwanathan, & R. Garnett, 5523–5533
- Treu, T. 2010, Annual Review of Astronomy and Astrophysics, 48, 87, arXiv: [1003.5567](#), doi: [10.1146/annurev-astro-081309-130924](#)
- Uria, B., Côté, M.-A., Gregor, K., Murray, I., & Larochelle, H. 2016, ArXiv e-prints, arXiv: [1605.02226](#)
- van den Oord, A., Kalchbrenner, N., & Kavukcuoglu, K. 2016a, ArXiv e-prints, arXiv: [1601.06759](#)
- van den Oord, A., Kalchbrenner, N., Vinyals, O., et al. 2016b, ArXiv e-prints, arXiv: [1606.05328](#)
- van den Oord, A., Dieleman, S., Zen, H., et al. 2016c, ArXiv e-prints, arXiv: [1609.03499](#)
- van der Walt, S., Colbert, S. C., & Varoquaux, G. 2011, Computing in Science and Engineering, 13, 22, arXiv: [1102.1523](#), doi: [10.1109/MCSE.2011.37](#)
- Van Tilburg, K., Taki, A.-M., & Weiner, N. 2018, JCAP, 2018, 041, arXiv: [1804.01991](#), doi: [10.1088/1475-7516/2018/07/041](#)
- Vegetti, S., Koopmans, L. V. E., Bolton, A., Treu, T., & Gavazzi, R. 2010, MNRAS, 408, 1969, arXiv: [0910.0760](#), doi: [10.1111/j.1365-2966.2010.16865.x](#)
- Vegetti, S., Lagattuta, D. J., McKean, J. P., et al. 2012, Nature, 481, 341, arXiv: [1201.3643](#), doi: [10.1038/nature10669](#)
- Verma, A., Collett, T., Smith, G. P., Strong Lensing Science Collaboration, & the DESC Strong Lensing Science Working Group. 2019, arXiv e-prints, arXiv:1902.05141, arXiv: [1902.05141](#)
- Vogelsberger, M., Zavala, J., Cyr-Racine, F.-Y., et al. 2016, MNRAS, 460, 1399, arXiv: [1512.05349](#), doi: [10.1093/mnras/stw1076](#)
- Vogelsberger, M., Zavala, J., & Loeb, A. 2012, MNRAS, 423, 3740, arXiv: [1201.5892](#), doi: [10.1111/j.1365-2966.2012.21182.x](#)
- Vogelsberger, M., Zavala, J., Schutz, K., & Slatyer, T. R. 2019, MNRAS, 484, 5437, arXiv: [1805.03203](#), doi: [10.1093/mnras/stz340](#)
- Wald, A. 1943, Transactions of the American Mathematical Society, 54, 426
- Warren, S. J., & Dye, S. 2003, The Astrophysical Journal, 590, 673, arXiv: [astro-ph/0302587](#), doi: [10.1086/375132](#)
- Wechsler, R. H., & Tinker, J. L. 2018, ARA&A, 56, 435, arXiv: [1804.03097](#), doi: [10.1146/annurev-astro-081817-051756](#)
- Wilks, S. S. 1938, Annals Math. Statist., 9, 60, doi: [10.1214/aoms/1177732360](#)
- Wong, K. C., Suyu, S. H., Chen, G. C. F., et al. 2019, arXiv e-prints, arXiv:1907.04869, arXiv: [1907.04869](#)
- Zahid, H. J., Sohn, J., & Geller, M. J. 2018, ApJ, 859, 96, arXiv: [1804.04492](#), doi: [10.3847/1538-4357/aabe31](#)
- Zavala, J., Vogelsberger, M., & Walker, M. G. 2013, MNRAS, 431, L20, arXiv: [1211.6426](#), doi: [10.1093/mnrasl/sls053](#)